Declustering *n*-connected components for segmentation of iodine implants in C-arm fluoroscopy images

Chiara Amat di San Filippo[5], Gabor Fichtinger[1], W. James Morris[2], Septimiu E. Salcudean[3], Ehsan Dehghan[4], Pascal Fallavollita[5]

[1]Queen's University, Kingston, Canada; [2]Vancouver Cancer Center, Vancouver, Canada; [3]University of British Columbia, Vancouver, Canada; [4]Philips Healthcare, New York, USA; [5]Technische Universität München, Germany

{filippo@in.tum.de, gabor@cs.queensu.ca, jmorris@bccancer.bc.ca, tims@ece.ubc.ca, ehsan.dehghan@philips.com, fallavol@in.tum.de}

Abstract. Dynamic dosimetry is becoming the standard to evaluate the quality of radioactive implants during brachytherapy. It is essential to obtain a 3D visualization of the implanted seeds and their relative position to the prostate. For this, a robust and precise segmentation of the seeds in 2D X-ray is required. First, implanted seeds are segmented using a region-based implicit active contour approach. Then, *n*-seed clusters are resolved using an efficient template based approach. A collection of 55 C-arm images from 10 patients are used to validate the proposed algorithm. Compared to manual ground-truth segmentation of 6002 seeds, 98.7% of seeds were automatically detected and declustered showing a false-positive rate of only 1.7%. Results indicate the proposed method is able to perform the identification and annotation processes of seeds on par with a human expert, constituting a viable alternative to the traditional manual segmentation approach.

1 Introduction

With an estimated 240,890 new cases in 2011, prostate cancer is the most common cancer among men in the United States, accounting for 29% of their cancers [1]. Brachytherapy, a definitive treatment for early stage prostate cancer, demonstrates excellent long-term disease-free survival and is chosen by over 60, 000 men annually. The brachytherapy procedure entails permanent implantation of small radioactive seeds, such as ^{125}I, ^{103}Pd, or ^{137}Cs, into the prostate to eliminate the cancer via radiation. Before the operation, the seed positions are planned using a transrectal ultrasound (TRUS) volume. The goal of the planning is to cover the target gland with a prescribed dose of radiation, while sparing the healthy surrounding tissue such as urethra and rectum. In current brachytherapy interventions, seed placement is performed under visual guidance from TRUS and further assessed with the acquisitions of multiple C-arm fluoroscopy images. Intraoperative dynamic dosimetry, the fusion of both TRUS and fluoroscopy data, would enable physicians to account for devia-

tions from the initial seeds placement plan and tailor the remaining dose so as to eradicate the cancer while minimizing harm to the surrounding healthy tissues [2].

1.1 Intra-operative dynamic dosimetry workflow

The following workflow closely reflects intraoperative dosimetry analysis and optimization (see Figure 1). The oncologist will acquire a number of transrectal ultrasound images until they feel it is time to verify implant position and dosimetric values. At that point, the acquired slices are compounded into a 3D volume. A C-arm fluoroscopy device is moved near the patient table and several X-ray images are acquired showing implant position. The C-arm images are pre-processed and the precise seed segmentations can be calculated using segmentation techniques. Next, seed correspondence between the acquired C-arm images is performed and subsequent 3D reconstruction of the seeds is realized as in [11]. The 3D ultrasound volume is then registered to the 3D seed reconstruction using a state-of-the art method as in [12, 13]. The oncologist can visually assess the multimodal fused data and determine whether there are under-dosed regions (cold spots) or regions with high risk of over-radiation. Lastly, dynamic dosimetry is inherently executed since the oncologist could change the planned position of the remaining seeds and add new seeds if required. To achieve suitable dynamic dosimetry intraoperatively precise seed segmentation must be achieved. Unfortunately, modern C-arm images are still afflicted with low signal-to-noise ratios and are characterized by illumination inhomogeneity [3]. Using thresholding algorithms would yield poor results [4]. Lastly, since many implants overlap— as many as five seed clusters in some scenarios— techniques to resolve these clusters into their constituent components need further investigation.

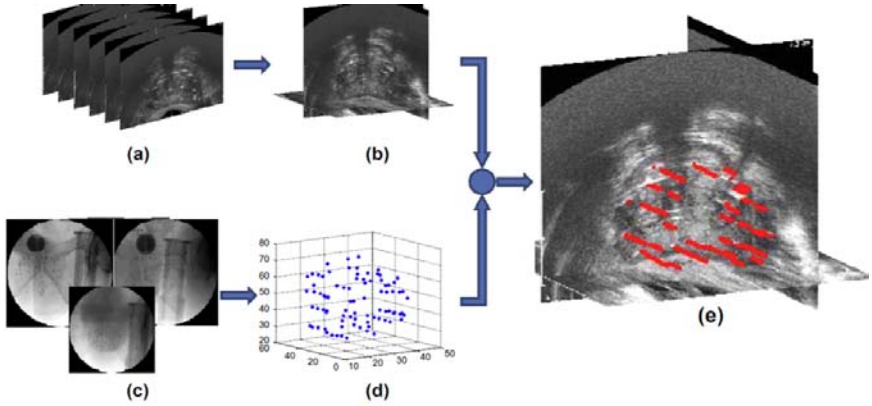

Figure 1. Dynamic dosimetry outline. (a): Several ultrasound images of the prostate. (b): 3D ultrasound volume. (c): C-arm images showing seeds. (d): Seeds reconstructed in 3D. (e): Registered seeds overlaid on the US volume. Seeds are shown as red capsules Image taken from the authors in [12].

1.2 Existing segmentation algorithms of implants

Brachytherapy seed segmentation in C-arm fluoroscopy images is a well-known topic in research practice [3-6]. For brevity, we summarize some of the key contributors in this topic. In Lam *et al*. [3], it is possible to observe the usage of a spoke transform to facilitate seed segmentation. In Tubic *et al.* [4], the morphological top-hat transform was used to normalize image illumination, in order to prepare the image for thresholding which was achieved through the bidimensional entropy method. Grouped pixels, thus potential seeds clusters, were identified using area, width, and length statistics of the clusters and subsequently declustered using a simulated annealing type algorithm. In Kuo *et al.* [5], a top-hat by reconstruction algorithm followed by thresholding via Otsu's method was employed. Overlapping seeds were identified- but not separated- by calculating the sum of the intensities of each pixel group and comparing it to the median sum. In the most recent state-of-the-art method, Moult *et al.* [6] used top-hat, Gaussian and Kirsch filters in combination. Afterwards, they used an implicit active contour algorithm to produce an image showing only the seeds. Finally, a declustering algorithm to decompose only two-seed clusters was introduced via a template-based scheme. All of the above works suffer from distinct limitations: (i) in [5] the authors consider only palladium seed segmentation, (ii) in all algorithmic steps require manual intervention for image cropping and definition of algorithm parameter thresholds and (iii) only n=2 seed clusters were accounted for which significantly reduces accuracy of seed reconstruction.

1.3 Contributions

According to Radiotherapy in Practice Brachytherapy: "*[t]he most frequently used isotope for permanent seed implantation in brachytherapy is iodine-125* [10]." Different implants require different segmentation schemes due to their shape and size—thus ^{103}Pd, or ^{137}Cs segmentation algorithms cannot be applied to iodine seeds which are longer in size. Consequently, the existing two-cluster solutions cannot be reduced for general clinical practice. It is clinically unacceptable to perform manual segmentation on the seeds, intra-operatively during the procedure, for every C-arm image of an implant (i.e. almost 5 seeds/C-arm image in [6]). This results in long procedure times and invites human operator errors. Clinical experience proves that n-cluster seed segmentation is required for a viable clinical implementation of intra-operative implant reconstruction and dosimetry. In this paper, a template matching technique that allows for fast and accurate n-seed cluster decomposition is proposed.

2 Implicit active contours and initial preprocessing

To segment the iodine brachytherapy implants, a region-based implicit active contour model by Li *et al.* [7] is used. Generally medical images have intensity inhomogeneity; hence the model proposed by Li *et al.* is suitable as it accounts for variances in image illumination and additionally eliminates the re-initialization process making this algorithm automatic. The initial segmentation can be summarized by the following four steps:

STEP 1: the X-ray image is filtered producing a processed image on which the active contour will be evolved. In this step, a morphological top-hat filter with rectangular structuring element is applied. The structuring element has dimension 12×2 pixels with longer y-axis length. We made the fitting assumption that implanted seeds in X-ray are rectangular in shape and closer to an upright orientation. It is impossible to insert and deposit a seed horizontally when guiding needle insertion using the needle template during brachytherapy.

STEP 2: the image that is used to initialize the active contour is generated here thereby eliminating the need for a manually defined ROI. This initialization image is formed using a top-hat filter, blurring the original X-ray with a Gaussian filter and employing a Kirsch edge filter [8]. For all trials the Kirsch filter threshold was $t_0 = 5$. Once the binarized edge image is formed, black-white (BW), the initial level set function ϕ^0 is defined as:

$$\phi^0(\mathrm{i},\mathrm{j}) = \begin{cases} -\mathrm{c}_0 & \text{if} \quad \mathrm{BW}(\mathrm{i},\mathrm{j}) = 1 \\ \mathrm{c}_0 & \text{elsewhere} \end{cases} \tag{1}$$

where $c_0 = 2$ as indicated in [7].

STEP 3: evolves the level set function for 70 iterations, after which a resulting binary image is obtained containing the seeds and possibly some lingering noise. For all trials, the energy functional parameters were set as those defined by the author in [7].

STEP 4: eliminates any remaining noise in the image. Connected regions < 20 pixels are discarded since their areas are below the assumed area of an implanted seed. Also, if the region width is larger than the region length, we discard as well, since implants are always closer to an upright position. Mean statistics are subsequently calculated similar to the state-of-the art method of [6]. Mean pixel area is determined by the number of pixels contained in all clusters. This value is divided by the number of connected components in the X-ray image. Lastly, regions of the image that deviate significantly from the mean statistics are removed. The statistics were formulated by analyzing the mean pixel area (MPA) of seed groups within X-ray images. The pixel groupings in this paper were set to [0.5, 5] times MPA. A value of five suggests at most 5 seed clusters whereas a value of ½ suggests the lower limit possibility of a region being a seed. This resulting image is used when applying the declustering algorithm described in the following section.

3 Declustering *n*-connected components

In the image, it is expected to find certain pixels that define two or more seed clusters. This fact motivates the introduction of seed declustering techniques to resolve such groupings. First, we briefly describe a method to reduce the search space as proposed

in [4, 6]. Second, we outline the steps involved in discerning the *n*-seed clusters based on area and length measures. Lastly, a general *n*-seed declustering scheme is outlined.

3.1 Search space reduction and cluster-discerning criteria

In order to make the declustering algorithm faster, a technique to reduce the search space within the C-arm images is introduced. The declustering technique is based on matching a set of template seeds to the overlapping seed group of interest [4]. The problem of this method is prohibitively large search space, hence to overcome this limitation, translation of the model template is not allowed and instead a set of 3 anchor points uniformly spaced in the shortest side of the pixel group is considered. This produces a search space reduced by over 99.96% [6]. In this paper, the clusters are identified and discriminated based on the area and length statistics of the clusters. We calculated the mean pixel area **A** (i.e. the area that a single seed should approximately have), calculated the mean pixel length **L** (i.e. the length that a single seed should approximately have and equal to the major axis length of the minimal enclosed bounding ellipse of the connected region). Then, we carefully selected the parameters $n_1 < n_2 < n_3 < n_4 < n_5 \in R$ and $m_1 < m_2 < m_3 < m_4 < m_5 \in R$ such that

- [(if $A \geq n_1 \cdot \mathbf{A}$) and ($A < n_2 \cdot \mathbf{A}$)] *or* [($l \geq m_1 \cdot \mathbf{l}$) and ($l < m_2 \cdot \mathbf{l}$)] – *two seed cluster*
- [(if $A \geq n_2 \cdot \mathbf{A}$) and ($A < n_3 \cdot \mathbf{A}$)] *or* [($l \geq m_2 \cdot \mathbf{l}$) and ($l < m_3 \cdot \mathbf{l}$)] – *three seed cluster*

The same reasoning is used to discern clusters of four and five seeds. In the implemented procedure the choice of values was determined empirically by analyzing a subset of C-arm images: $n_1=m_1= 1.3$; $n_2= m_2= 1.9$; $n_3=m_3= 3.1$; $n_4=m_4= 4.0$; $n_5=m_5=4.5$. Through these values all possible cluster shapes can be accounted for (i.e. Y-shape, etc.). We randomly selected a subset of 5 images to train and arrive at the above values. A visual inspection of the subset of images revealed seed projections having 'close enough' geometric similarities capturing population variability.

Template Seeds for matching: A template seeds are a rectangle of size 5 × 22 pixels (i.e. 1.0 x 4.4 mm using a pixel spacing equal to 0.2013mm) determined empirically by visualizing a sub-sample of projected seeds in the C-arm images. To achieve improved precision not just one template fixation point is used, but three, lying on the shortest side of the seed. A set of possible rotations $R = \{k \cdot (\pi/16) \rightarrow k \in 0, \ldots, 15\}$ is also considered and the templates which have the highest intersection with the pixel cluster is selected as the matching one.

3.2 *n*-seed declustering framework

The graphical outline of the procedure can be seen in Figures 2-3. The pixels of the *n*-seed cluster are labelled with the number **c**. The pixels p_1^* and p_n^* are defined as the most distant ones in the cluster (Figure 2a). Using the two-seed declustering algorithm in [6], the pixels p_1^* and p_n^* belong respectively to two different seeds clusters s_1 and s_n. The pixels belonging clusters s_1 and s_n are detected (Figure 2b) and only the ones belonging to s_n and relabelled with the number **c + 1**. The remaining pixels belonging to the original cluster stay untouched and the cluster is now composed of (*n*

− 1) seeds (Figure 3a). Before starting the next iteration just the connected component of the cluster is selected, (see Figure 4). The two-seed declustering algorithm is applied on the connected component of the cluster, and the pixels p_1^* and p_{n-1}^* belong respectively to two different seeds of the cluster s_1 and s_{n-1}.

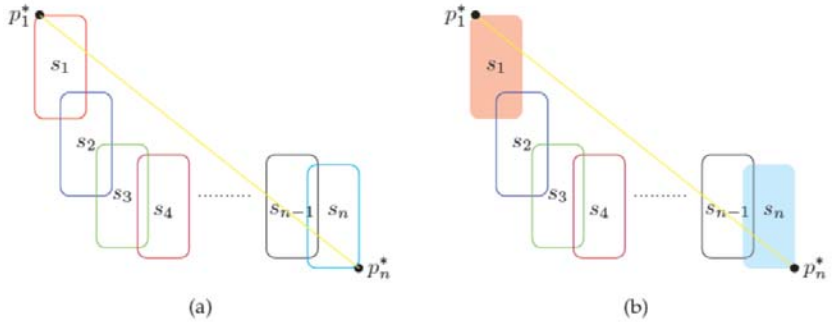

Figure 2. (a) Cluster of *n* seeds, the points p_1^* and p_n^* are the most distant in the cluster, they belong respectively to seed s_1 and s_n. (b) Seeds s_1 and s_n are detected.

The pixels belonging to s_{n-1} are detected and relabelled with the number **c + 2**. At step *k*, seed s_1 and s_{n-k+1} will be detected with the two-seed declustering algorithm, and only s_{n-k+1} is relabelled with number **c + k**. This procedure is repeated $n - 1$ times. In the last step $k = n - 1$, the most distant pixels p_1^* and p_2^* belong respectively to the last two seeds of the cluster s_1 and s_2 (see Figure 3b). Consequently, the two-seed declustering can be used and the original *n*-seed cluster has been successfully declustered.

We observe that seed s_1 has been detected $n - 1$ times using template matching and this is an unwanted side-effect of the algorithm and leaves open space for further improvements. In this paper, this problem does not affect the computational cost as we consider only cases in which $n \leq 5$. An improved version of the generalized n-seed declustering algorithm follows. In every iteration *k* of the algorithm, the pixels belonging to seeds s_1 and s_{n-k+1} are relabeled with numbers **c + 2k − 1** and **c + 2k**.

In each step, 2 seeds are extracted from the cluster enabling only $\left\lceil \frac{n-1}{2} \right\rceil$ iterations. The last step will be different for the case of *n* being an even or odd number: if *n* is odd, there is only one remaining seed labeled with **c** → end algorithm; *n* is even signifying there are two seeds remaining labeled with **c**→ apply the two-seed algorithm. For brevity, the workflow of a three-seed declustering framework is presented in Figure 4 and shown iteratively using a preprocessed clinical scenario.

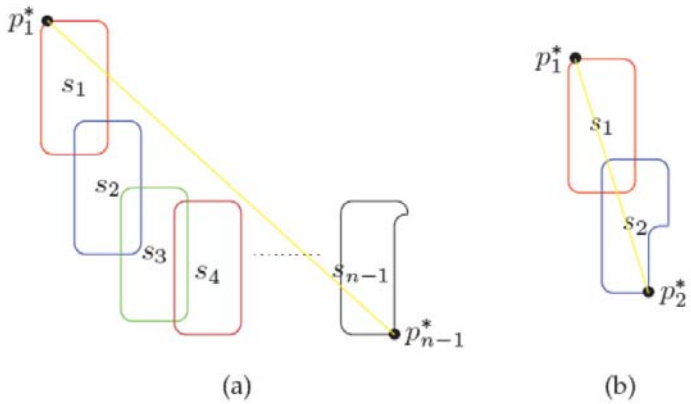

Figure 3. (a) Seed s_n is relabeled and the cluster is formed only from seeds s_1 to s_{n-1}. The most distant points in the cluster are now p_1^* and p_{n-1}^*. (b) The procedure is applied until only two seeds remain at which point [6] is applied.

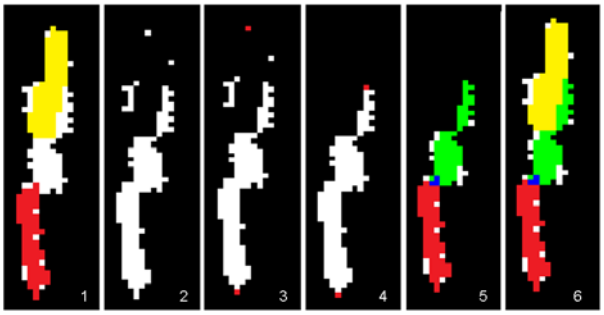

Figure 4. Declustering workflow for a three-seed grouping. (1) A three-seed cluster where the two most distant seeds are detected using a two-seed clustering technique. (2) One of the seeds is relabeled (i.e. it does not belong to the cluster anymore). (3) The most distant points u* and v* are wrongly selected. (4) The most distant points u* and q* are now correctly selected considering just the connected component of the pixel cluster. (5) The two-seed algorithm is applied again. (6) The three-seed declustering is now complete.

4 Evaluation and Results

Datasets: We validated the proposed segmentation and declustering method on 55 clinical images from 10 patients. One observer segmented the iodine seeds in the clinical images. As per all manual segmentation tasks, the general rule was to select the center point of a seed to the best of their ability. A total of 6002 seed centroids were manually segmented and these are considered the ground-truth seed coordinates for comparison.

Processing: The algorithm was prototyped in a MATLAB/C++ environment having a runtime of 50 seconds per C-arm image using an Intel®Core™ i7 computer.

Results: In total, 5918 seeds were automatically segmented using our method which results in a 98.7% detection rate. Our calculations using a 95% confidence interval, with $p<0.05$, returns 0.448. Thus, the high and low intervals around our mean detection rate are [98.14, 99.04]. The proposed *n*-seed declustering algorithm found 554 two-seed clusters, 68 three-seed clusters, 2 four-seed clusters and 1 five-seed cluster. These results were compared to the ground truth clusters, that were respectively 511 two-seed clusters, 56 three-seed clusters, 3 four-seed clusters and 0 five-seed cluster, confirming that the presented method responds quite well for overlapping iodine seeds. In order to evaluate the precision of our algorithm the mean centroid error was calculated. The overall mean centroid error between ground-truth manual and automatic segmentations was 1.2 pixels, or 0.24mm when considering our pixel spacing of 0.2013mm. Due to the GUI used for the seed centroid extraction, manually segmented seeds could only be placed at the centers of the image pixels. Since the distance from the center of a pixel to one of its corner is equal to sqrt (0.5), we define this value as the pixel uncertainty associated with the manual segmentations. However, these results re-affirm the efficacy of the proposed algorithm.

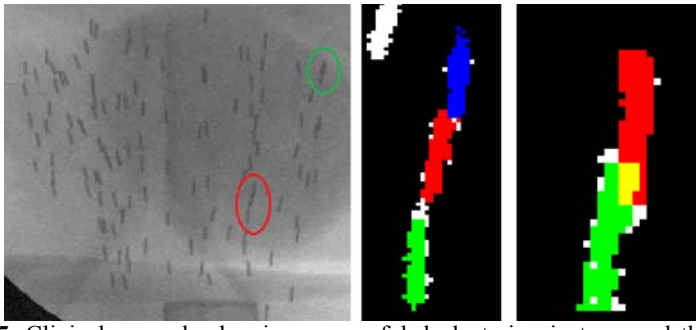

Figure 5. Clinical example showing successful declustering in two- and three-seed clusters. (*Left*) the input X-ray image on the left is displayed, in red the three seed cluster is highlighted, in green the two-seed cluster. (*Right*) the detection of the seeds belonging to the three- and two- seed clusters respectively.

Clinical Implications: In reference to the D90 values—the minimum dose received by 90% of the prostate volume—Su *et al.* [9] state "*[t]he 95% confidence interval (CI) of estimated D90 values differ by less than 5% from the actual value when 95% or more seeds are detected, or approximately a 7 Gy difference in the D90 value for a prescription dose of 144 Gy*." They concluded that accurate dose estimation can be achieved if 95% or more seeds are detected. Thus, our mean automatic detection rate of 98.7% surpasses clinical standards. Regarding segmentation, 84 seeds were not detected by our algorithm yielding an average of only 1.5 missed seeds per patient-image. Our results demonstrate a viable solution in the workflow of dynamic dosimetry (Figure 1) that ensures subsequent seed reconstruction in 3D and registration to TRUS data.

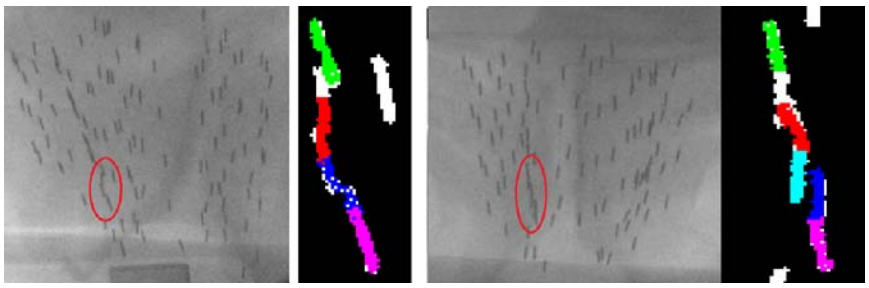

Figure 6. Clinical examples depicting successful declustering of four-seed cluster on the left image and a false clustering of five-seeds in the right image.

Drawbacks: 103 seeds were erroneously segmented, leading to a 1.7% false positive rate. This signifies that these were recognized by our algorithm as seeds; however they had no associated manual segmentation ground-truth. Here, it is observed that some identified clusters are not true clusters but a result from errors in the level set evolution (Figure 6-right), there is in fact two distinct clusters and not a five-seed cluster– a two- and three seed group).

Future Work: We aim at investigating filtering techniques, such as the homomorphic filter, that improves the original contrast of a newly acquired C-arm image during brachytherapy. We want to provide an initial image that optimizes the chances of the level set algorithm to lock onto seeds instead of *noisy* pixels. A natural extension of our algorithm is regarding the segmentation of other implants, such as ^{103}Pd or ^{137}Cs, which are used in prostate brachytherapy procedures. Also, color-coding the grayscale C-arm image which depicts individual or clustered seeds may facilitate seed correspondence between images for subsequent 3D reconstruction (Figure 7).

5 Conclusions

In this work we have presented a practical technique to robustly segment prostate brachytherapy iodine implants thereby making an important contribution to both research and clinical practice. We have improved current state-of-art algorithms by proposing an *n*-seed declustering scheme for iodine seeds and positively validated the technique on patient datasets.

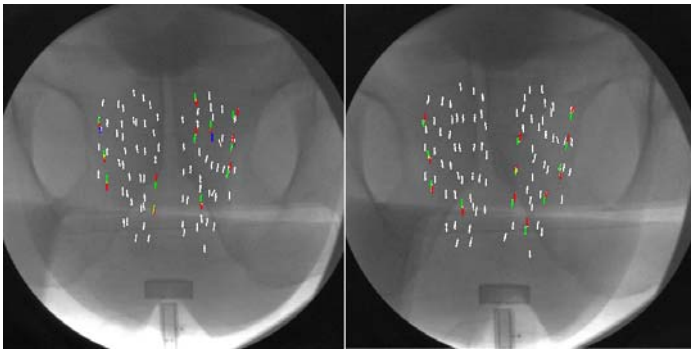

Figure 7. C-arm imaged of the same patient showing clusters and individual seeds. A side benefit from colored segmentations: simplified seed correspondence.

References

1. Siegel, R., Ward, E., Brawley, O., Jemal, A.: 2011 Cancer statistics CA: Cancer J. Clin. 61 (4), 212–236 (2011)
2. S. Nag, J. P. Ciezki, R. Cormack, S. Doggett, K. DeWyngaert, G. K. Edmundson, R. G. Stock, N. N. Stone, Y. Yu, and M. Zelefsky.: Intraoperative planning and evaluation of permanent prostate brachytherapy: report of the American brachytherapy society. International Journal of Radiation Oncology Biology Physics 51(5), p. 1422 (2001)
3. S. Lam, R. J. Marks, and P. S. Cho.: Prostate brachytherapy seed segmentation using spoke transform. in SPIE, 4322(1), pp. 1490–1500 (2001)
4. D. Tubic, A. Zaccarin, L. Beaulieu, and J. Pouliot.: Automated seed detection and three-dimensional reconstruction. i. seed localization from fluoroscopic images or radiographs. Medical Physics 28(11), pp. 2272–2279 (2001)
5. N. Kuo, N., Deguet, A., Song, D.Y., Burdette, E.C., Prince, J.L., Lee, J.: Automatic segmentation of radiographic fiducial and seeds from x-ray images in prostate brachytherapy. Med. Eng. Phys. 34 (1), pp. 64–77 (2012)
6. E. Moult, G. Fichtinger, W. Morris, T. Salcudean, E. Dehghan, and P. Fallavollita.: Segmentation of iodine brachytherapy implants in fluoroscopy. IJCARS 7(6): pp.871-9 (2012)
7. C. Li, C. Kao, J. C. Gore, and Z. Ding.: Minimization of region-scalable fit- ting energy for image segmentation. IEEE Transactions on Image Processing 17, pp. 1940–1949 (2008)
8. R. A. Kirsch.: Computer determination of the constituent structure of biological images. Computers and Biomedical Research, 4, pp. 315–328 (1971)
9. Y. Su, B. Davis, M. Herman, A. Manduca, and R. Robb.: Examination of dosimetry accuracy as a function of seed detection rate in permanent prostate brachytherapy. Med Phys 32: pp.30493056 (2001)
10. Hoskin P, Coyle C. Radiotherapy in Practice - Brachytherapy. Radiotherapy in Practice Series, Oxford University Press (2011)
11. Lee, J., C. Labat, A. K. Jain, D. Y. Song, C. E. Burdette, G. Fichtinger, and J. L. Prince.: REDMAPS: Reduced-Dimensionality Matching for Prostate Brachytherapy Seed Reconstruction. IEEE Transactions on Medical Imaging, vol. 30, issue 1, pp. 38-51 (2011)
12. P. Fallavollita, Z. KarimAghaloo, EC Burdette, DY Song, P. Abolmaesumi, G. Fichtinger.: Registration between ultrasound and fluoroscopy or CT in prostate brachytherapy. Medical Physics, 37(6): pp. 2749-60. (2010)
13. Dehghan, E., J. Lee, P. Fallavollita, N. Kuo, A. Deguet, Y. Le, C. E. Burdette, D. Y. Song, J. L. Prince, and G. Fichtinger.: Ultrasound–fluoroscopy registration for prostate brachytherapy dosimetry. Medical Image Analysis, vol. 16, issue 7, pp. 1347-1358 (2012)